Supplementary Information (SI) for Journal of Materials Chemistry A.
This journal is © The Royal Society of Chemistry 2026

Supporting Information

Fragment of Polymers with Z-scheme-like Electron Transfer Mechanism Driven by Multiple Built-in Electric Fields for Photocatalytic H_2O_2 Production

Huijie Wang[1,11], Yani Liu[2,11], Yitian Peng[1], Yaqi Hao[1], Hao Yang[1], Shenao Wang[1], Jinming Ye[1], Jun Luo[1*]

[1] State Key Laboratory of Featured Metal Materials and Life-cycle Safety for Composite Structures, MOE Key Laboratory of New Processing Technology for Nonferrous Metals and Materials, and School of Resources, Environment and Materials, Guangxi University, Nanning 530004, China.

[2] Key Laboratory of Water Pollution Control Technology, Hunan Research Academy of Environmental Sciences, Changsha 410004, China

[11]These authors contributed equally: Huijie Wang, Yani Liu

*E-mail address: junluo@gxu.edu.cn

Measurement of photocurrent and surface photovoltage

The electrochemical workstation (CHI760E) was used to measure the EIS Nyquist spectrum and transient photocurrent. Preparation of the working electrodes was as follows: 10 mg photocatalyst was dispersed in a mixture solution of 1 mL Nafion perfluorinated resin solution and 1 mL ethanol. 20 μL of resultant suspension was uniformly dropped onto the surface of a 2 cm^2 Indium-Tin Oxide plate. The electrode system consists of a working electrode (ITO coated with a fixed amount of photocatalyst), a carbon rod as a counter electrode, and an Ag/AgCl electrode as a reference electrode, of which 0.1 M Na_2SO_4 was used as electrolyte[1].

Rotating Ring-Disk Electrode (RRDE) Measurements

RRDE measurements were performed with an electrochemical workstation (Chenhua CHI 760E). The ring potential of the ring-disk electrode was sustained at 1.48 V (vs RHE). The Ag/AgCl electrode and carbon rod were employed as the reference and counter electrodes, respectively. The linear sweep voltammetry curves were acquired in an O_2-saturated 0.10 M phosphate buffer solution. The number of transferred electrons was calculated using the following equation:

$$n = 4\frac{I_d}{I_d + \frac{I_r}{N}} \qquad \text{* MERGEFORMAT (1)}$$

where I_d is the disk current, and I_r is the ring current. The collection efficiency (N) is determined to be 37%.

Photocatalytic performance measurement

The catalyst (50 mg) was uniformly dispersed into mixed solution containing 5mL of acetic acid and 45 mL of water with ultrasonication for 30 min. Then, the suspension solutions were stirred for 30 min with continual O_2 bubbling in the dark to reach the absorption−desorption equilibrium. The light source used was a 300 W xenon lamp (PLS-SXE300D/300DUV, Beijing Perfectlight) with 420 nm cutoff filter. The distance between the reactor and the light source is 15 cm, and the solutions were kept stirring during the experiment. At certain time intervals, 3 mL of suspension was sampled and centrifuged to remove the photocatalysts. The amount of H_2O_2 was measured by

iodometry[2].

Photocatalyst recovery and cycling experiments

After the photocatalytic production of hydrogen peroxide experiment, the photocatalyst was separated from the solution through a vacuum filter and a water-based filter membrane with a pore size of 0.22 μm. Subsequently, it was placed in an oven at 60 °C for 12 h to obtain dry samples for different cycles to study its cycling stability.

The determination of reactive species

In the photoactive species capture experiments, 2 mM p-benzoquinone (PBQ) and 2 mM L-histidine were used as the scavenger for •O− 2 and $^1O_2$, respectively. All scavengers were dissolved into the mixed solution containing 5 mL of ethanol and 45 mL of water to be degraded prior to the experiment.

Energy level calculation

$$(ahv)^{\frac{1}{n}} = A\left(hv - E_g\right) \qquad \text{* MERGEFORMAT (2)}$$

$$E_{VB} = \Phi + VB_{max} - 4.44 \qquad \text{* MERGEFORMAT (3)}$$

$$E_{CB} = E_{VB} - E_g \qquad \text{* MERGEFORMAT (4)}$$

Where α, h, A, μ, E_g and n are the energy-dependent absorption coefficient, representing the Planck constant, the band gap width, the absorption constant, the forbidden bandwidth, and the constant value of the semiconductor transition, respectively[3]. Φ is the electron work function of the analyzer (4.2 eV), and VB_{max} is the VB potential[4].

Built-in electric field calculation

$$F_s = \left(\frac{-2V_s\rho}{\varepsilon\varepsilon_0}\right)^{\frac{1}{2}} \qquad \text{* MERGEFORMAT (5)}$$

Where F_s represents the built-in electric field strength, V_s is the surface potential,

ρ denotes the surface charge density, ε is the low-frequency dielectric constant, and ε_0 is the free-space dielectric constant[5, 6].

Calculation of dipole moment

The molecular dipole moment (μ) is a vector quantity, with its direction pointing from the center of positive charge to the center of negative charge[7]. Its magnitude is calculated via the vector summation of the partial charges (q_i) of all atoms within the molecule and their respective position vectors (r_i). In this study, q_i was obtained through Mulliken charge analysis, and r_i was determined by measuring the distance between charge centers using the VESTA software.

$$\mu = \Sigma q_i r_i \qquad \backslash* \text{ MERGEFORMAT (6)}$$

Where μ denotes the dipole moment vector, q_i is the magnitude of charge and r_i is the distance between the positive and negative charge centers.

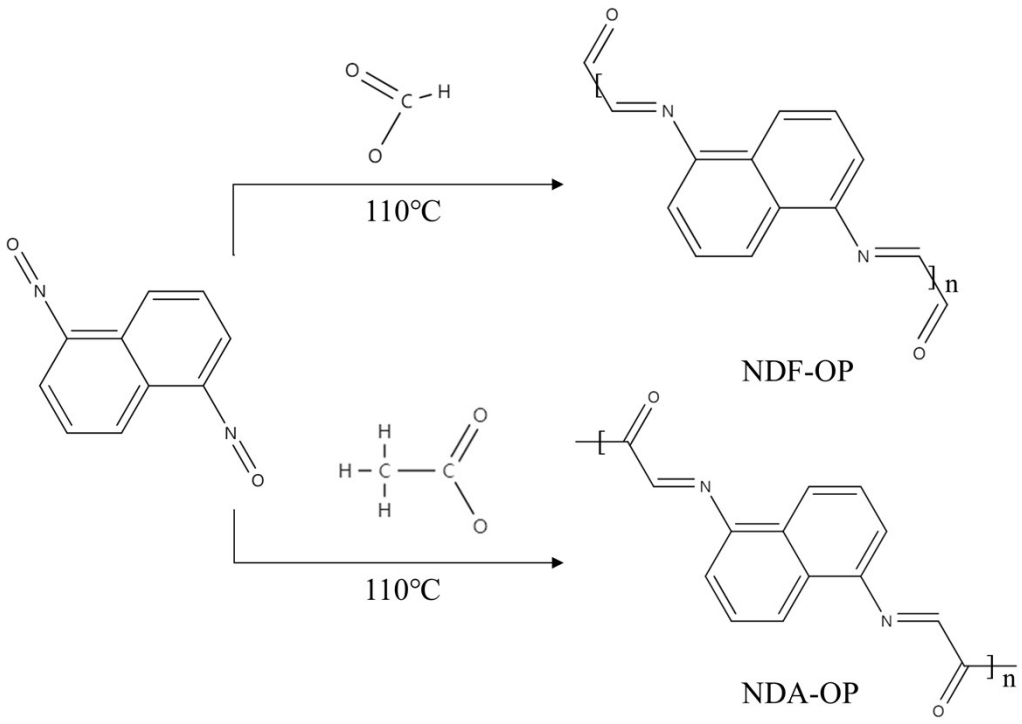

85

86 **Scheme S1.** The synthetic routes for NDF-OP and NDA-OP composite.

87

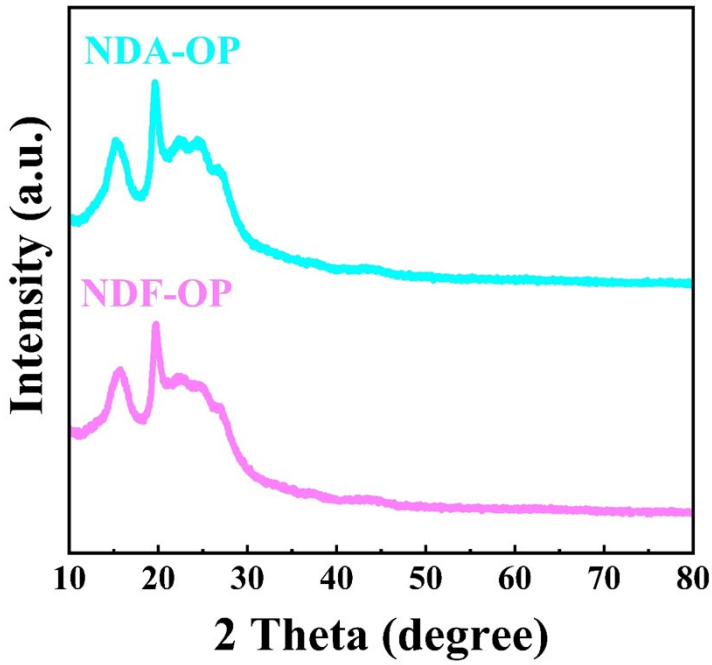

88

89 **Figure S1.** XRD patterns of NDF-OP and NDA-OP.

90

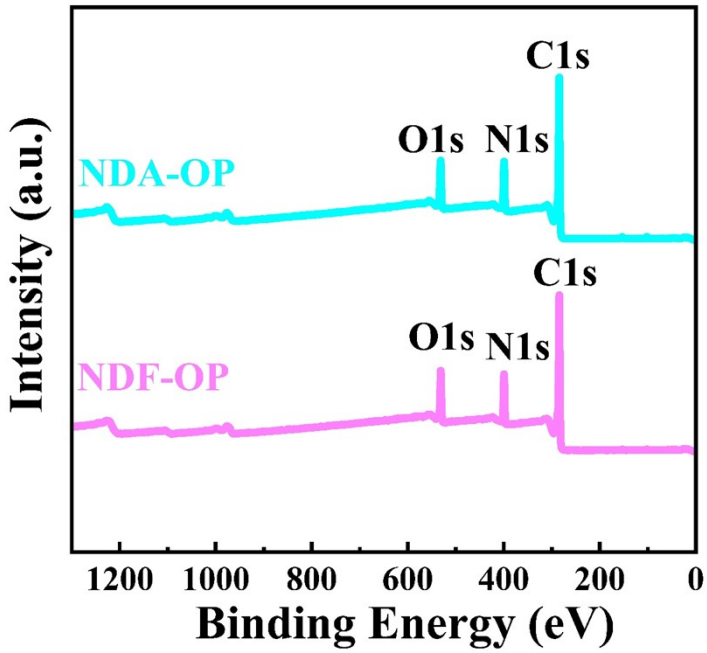

91
92 **Figure S2.** XPS survey of NDF-OP and NDA-OP.

93

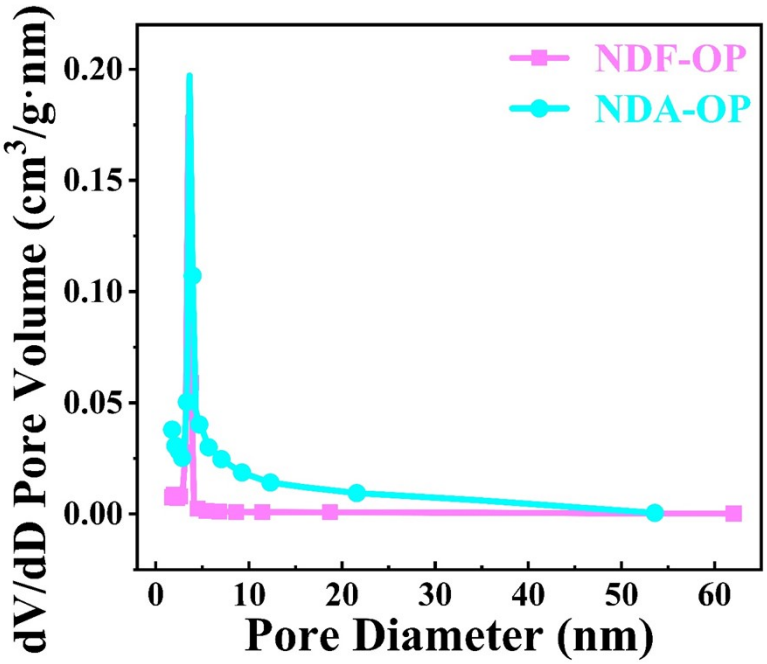

94
95 **Figure S3.** Pore size distributions of NDF-OP and NDA-OP.

96

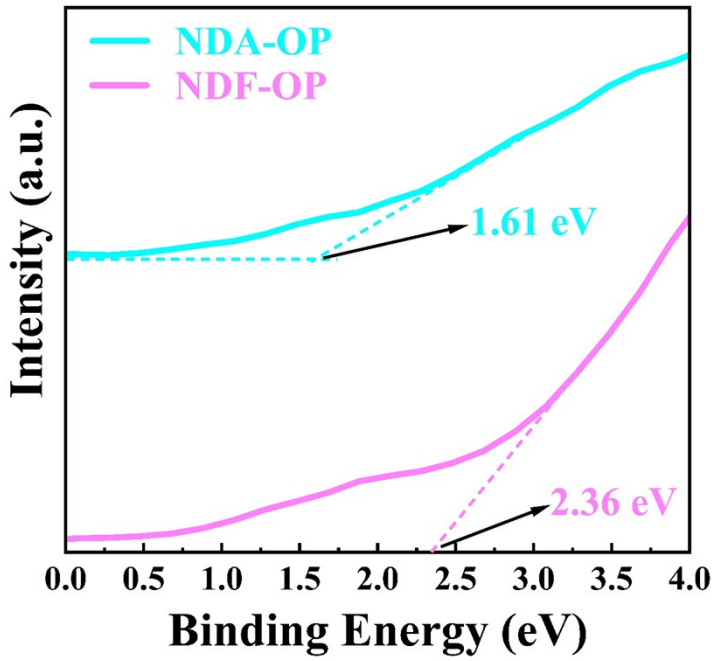

Figure S4. VB spectra of NDF-OP and NDA-OP.

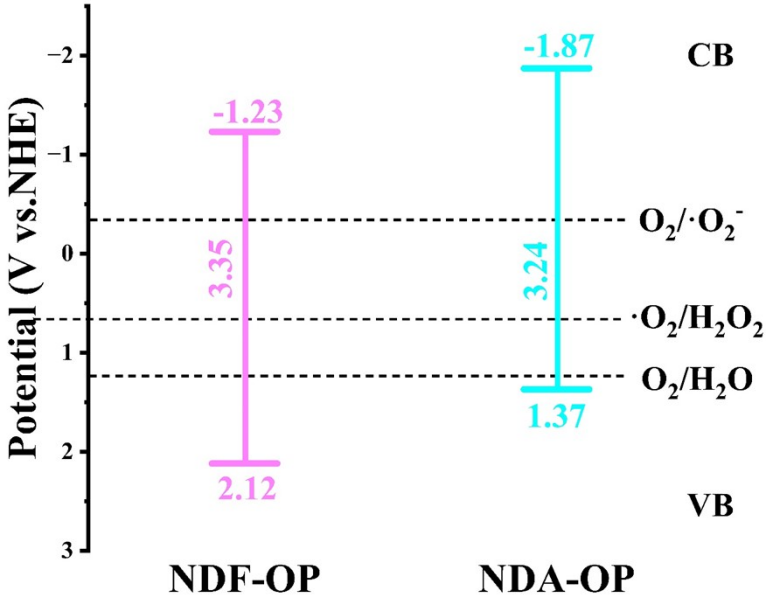

Figure S5. Energy band structures of NDF-OP and NDA-OP.

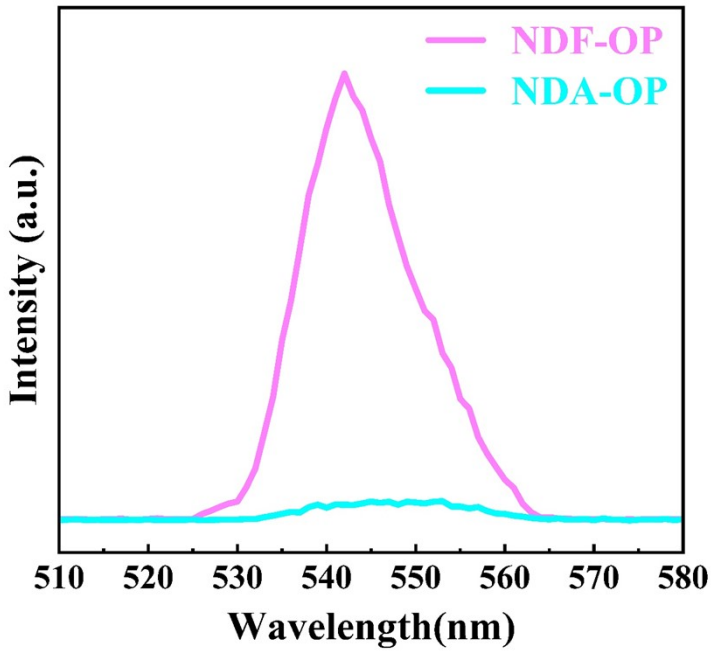

Figure S6. PL spectra of NDF-OP and NDA-OP.

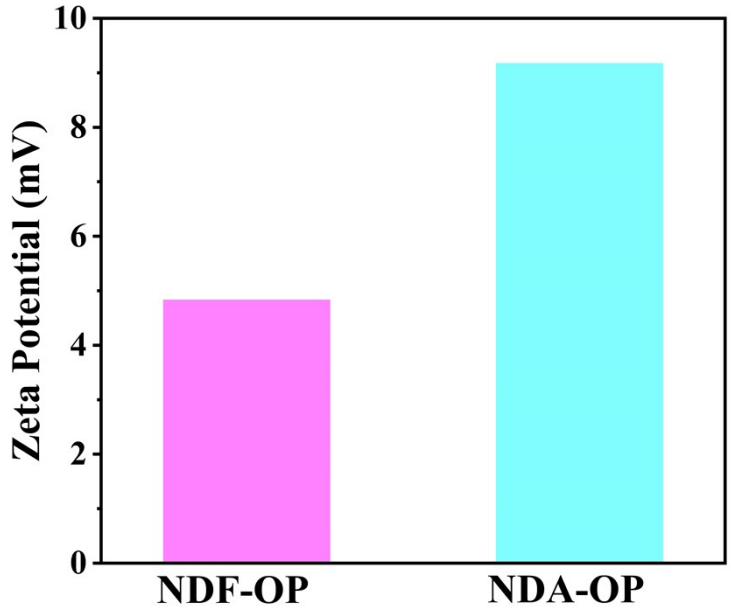

Figure S7. Zeta potential of NDA-OP and NDF-OP.

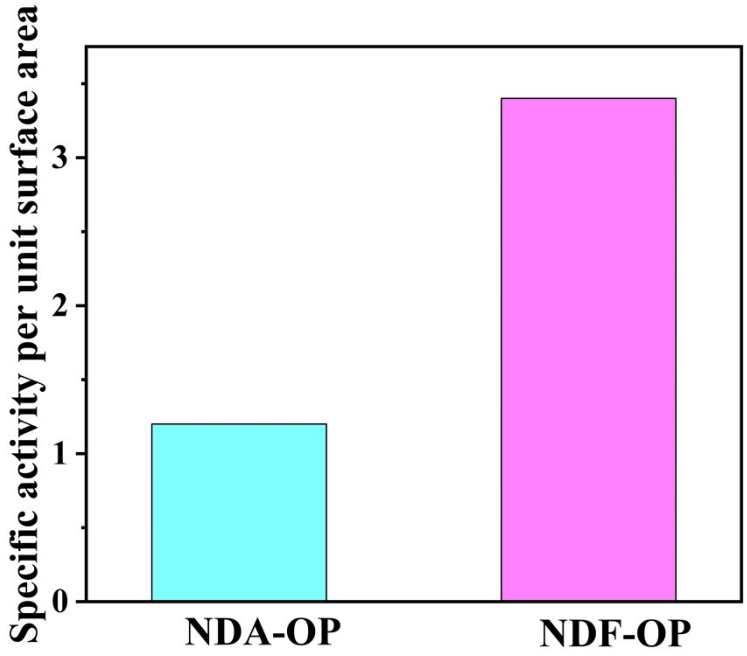

Figure S8. Specific activity per unit surface area of NDA-OP and NDF-OP.

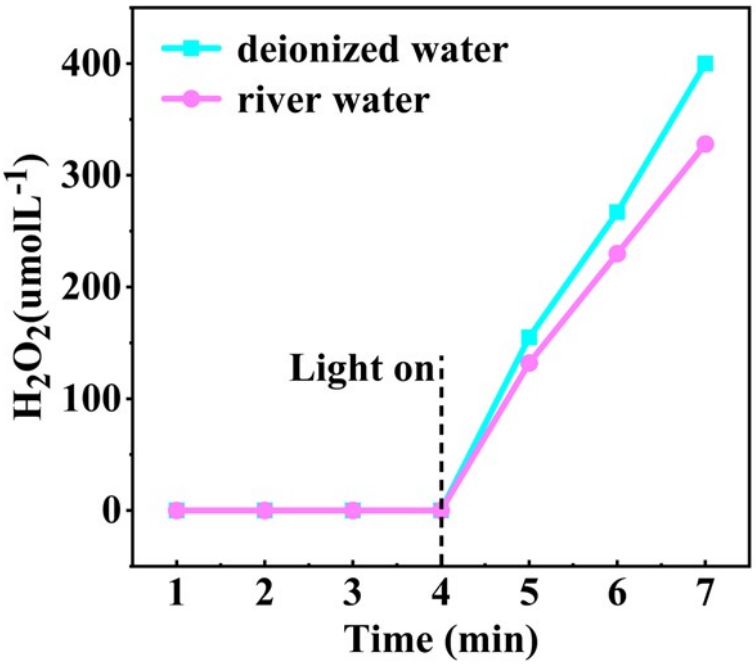

Figure S9. The photocatalytic production of H_2O_2 in deionized water and real water under visible light irradiation ($\lambda > 420$ nm) and a saturated O_2 atmosphere.

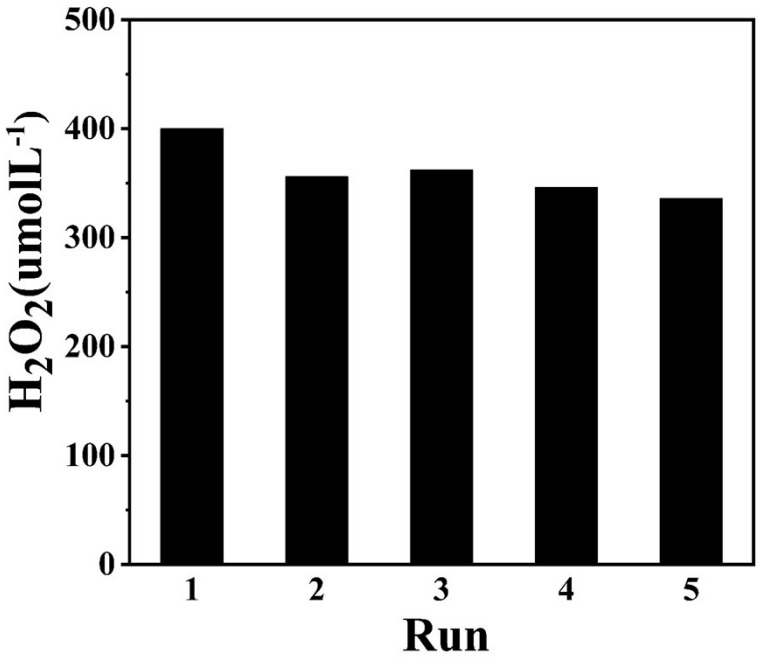

Figure S10. The photocatalytic generation of H_2O_2 by NDA-OP for five times with 10% alcohol under visible light irradiation and a saturated O_2 atmosphere.

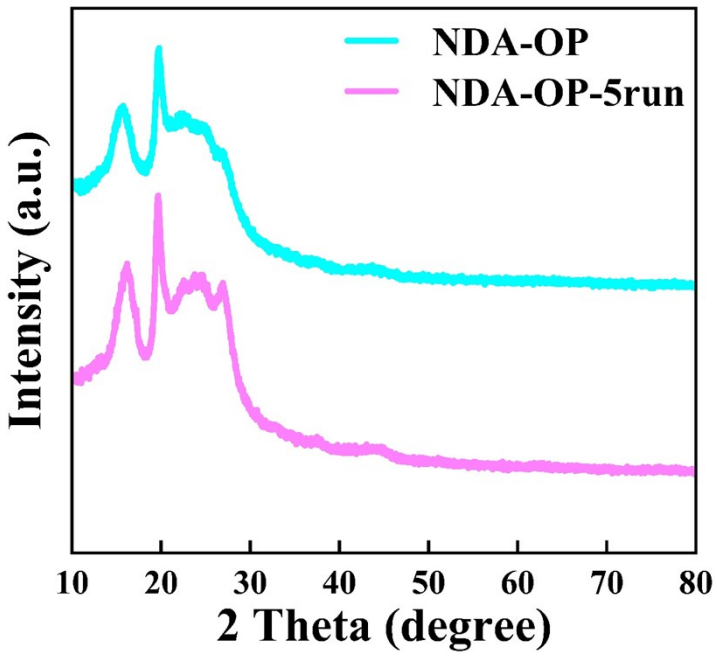

Figure S11. XRD pattern of the prepared NDA-OP before and after the photocatalytic production of H_2O_2.

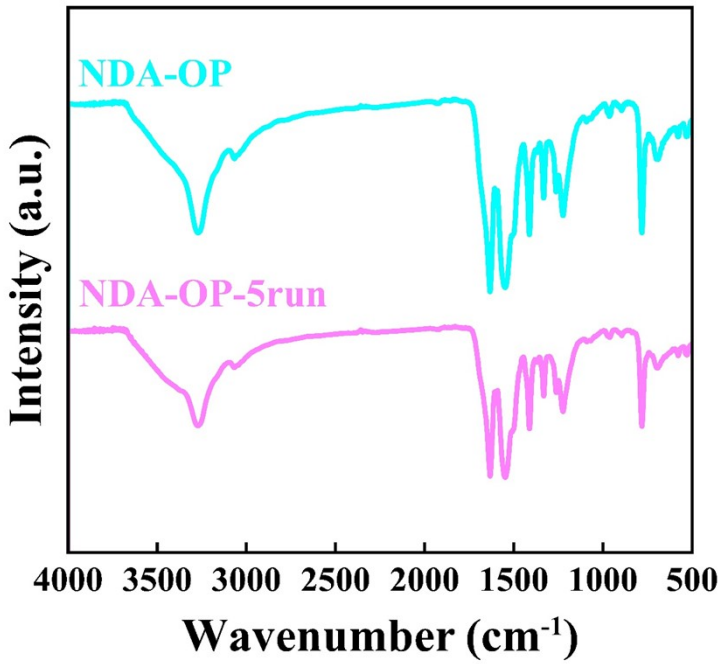

123

124 **Figure S12.** FTIR pattern of the prepared NDA-OP before and after the photocatalytic

125 production of H_2O_2.

126

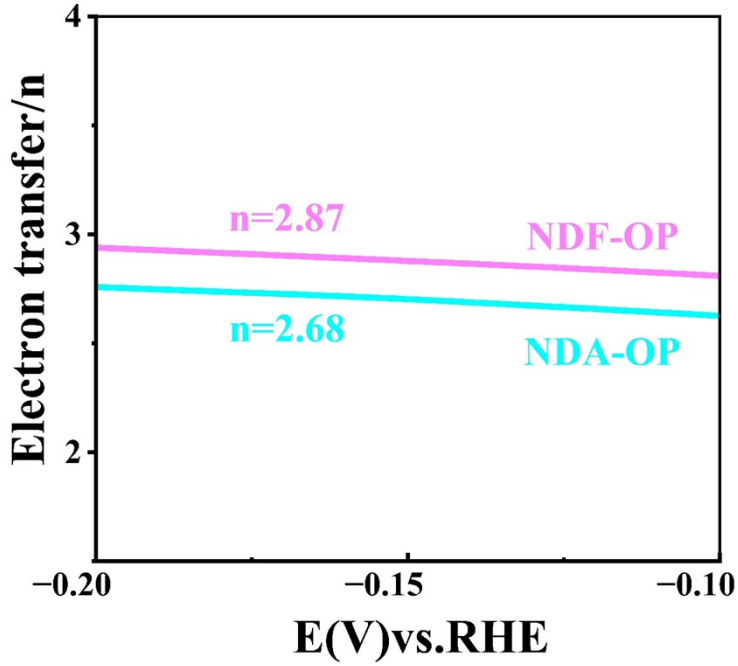

127

128 **Figure S13.** Electron transfer numbers at different potentials calculated from RRDE

129 data.

130

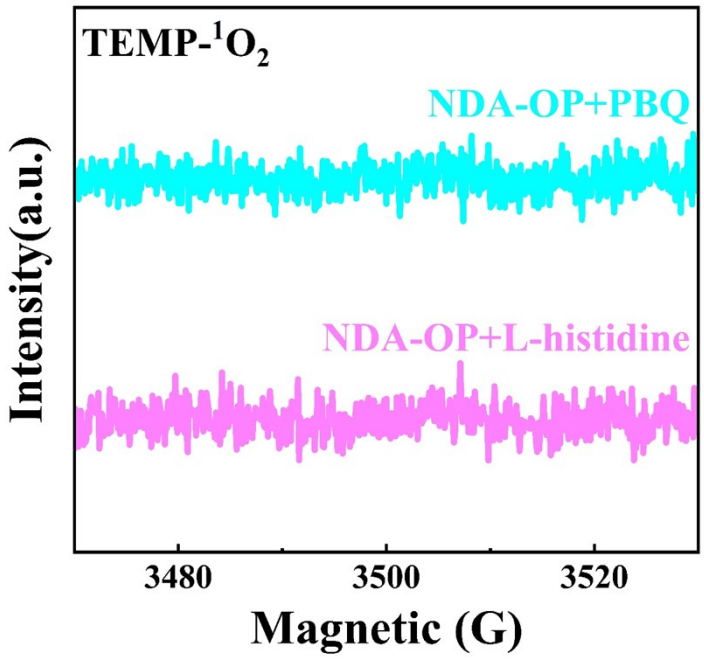

131
132 **Figure S14.** ESR spectra of TEMP-$^1O_2$ adduct for NDA-OP with PBQ and L- histidine
133 under visible-light illumination.

134

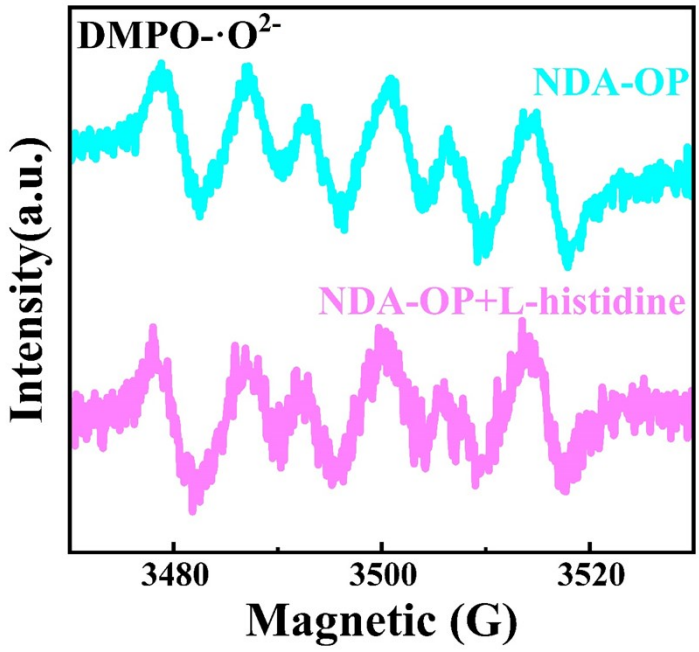

135
136 **Figure S15.** ESR spectra of DMPO-•O_2^- adduct for NDA-OP with and without L-
137 histidine under visible-light illumination.

138

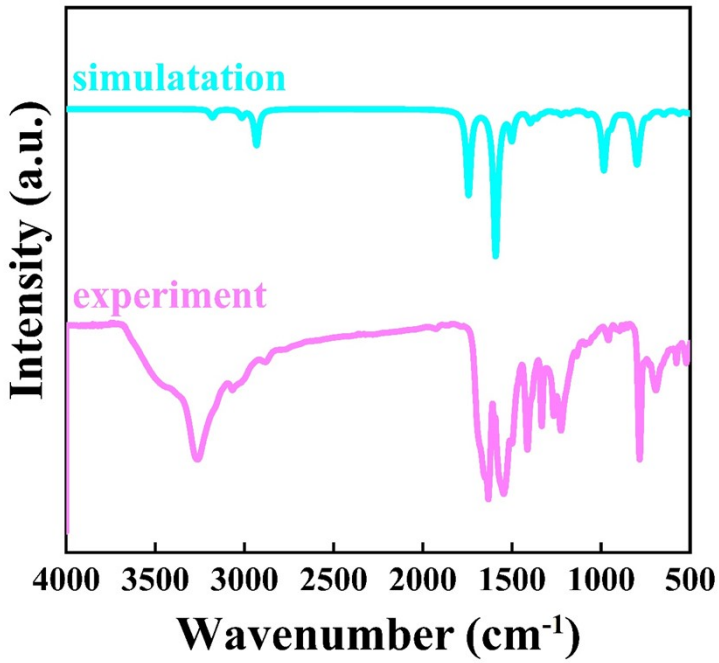

Figure S16. Experimental FTIR spectra and simulated FTIR spectra of NDA-OP.

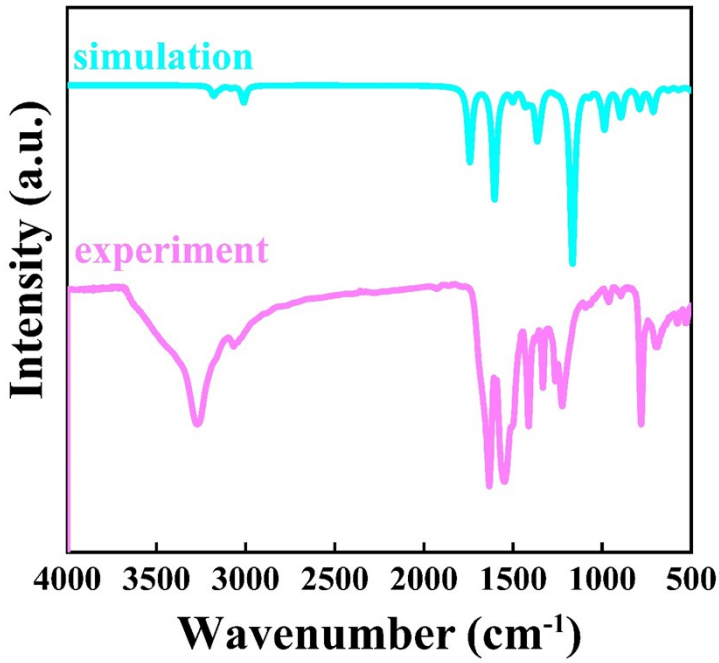

Figure S17. Experimental FTIR spectra and simulated FTIR spectra of NDF-OP.

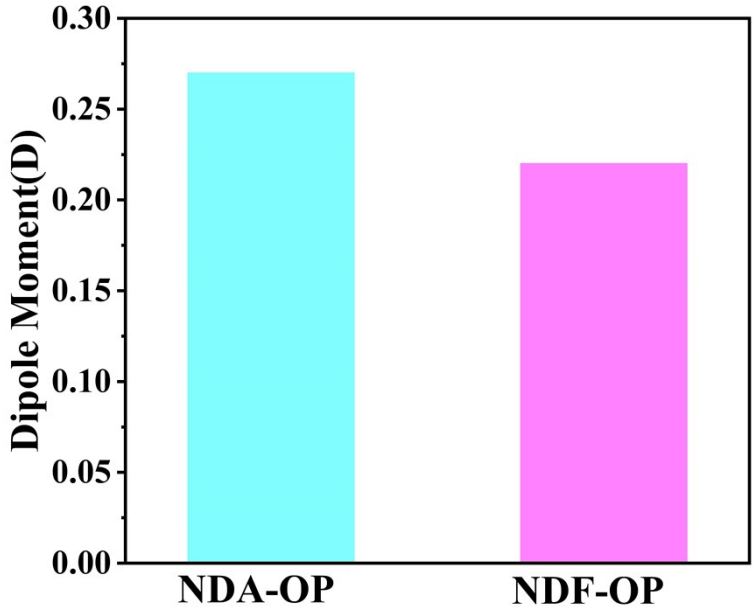

Figure S18. Dipole moments of NDA-OP and NDF-OP.

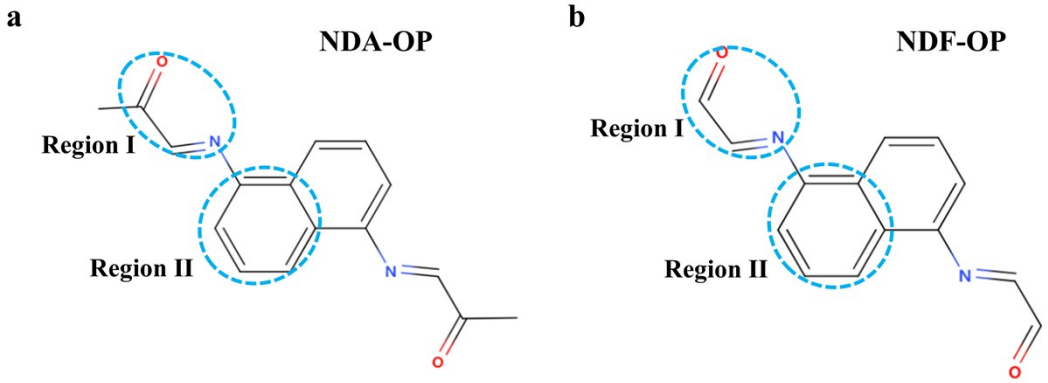

Figure 19. Structural formula of (a) NDA-OP and (b) NDF-OP, respectively.

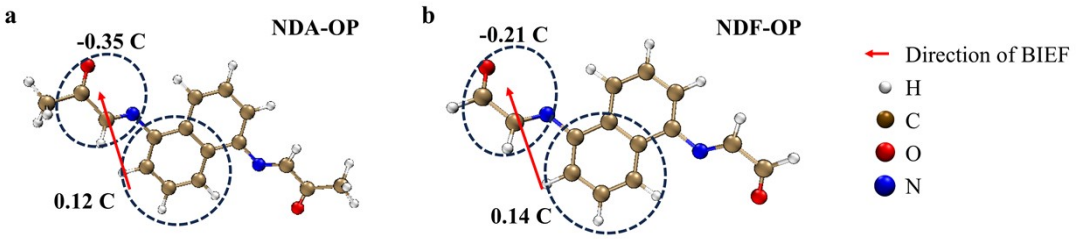

Figure S20. Local atomic charge diagram and BIEF direction of (a) NDA-OP and (b) NDF-OP, respectively.

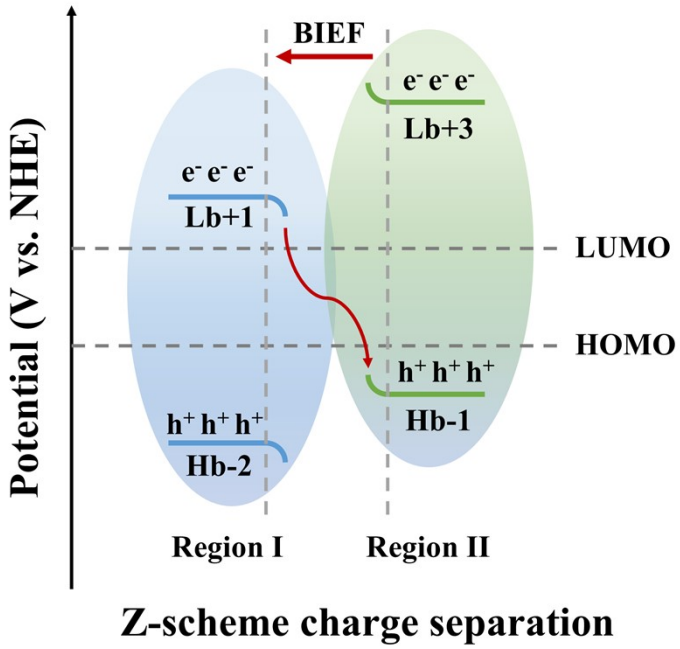

Figure S21. Energy level transition diagram of NDA-OP.

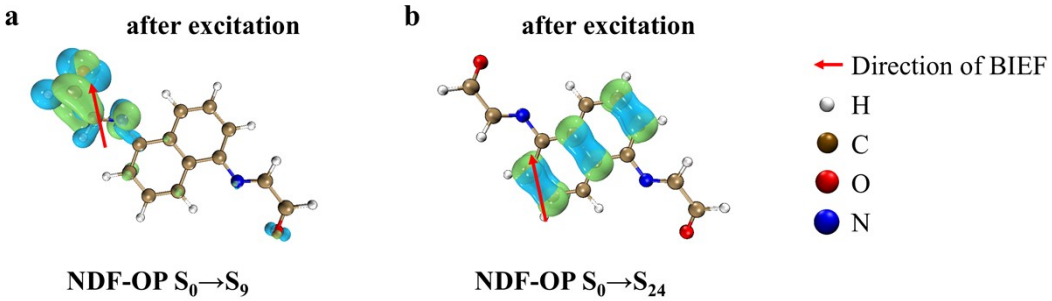

Figure S22. The electron-hole distribution of NDF-OP for (c) $S_0 \rightarrow S_9$ and (d) $S_0 \rightarrow S_{24}$ excitations, respectively. Green represents the electron distribution and blue represents the hole distribution. The isosurface value is 0.003 e/Å^3.

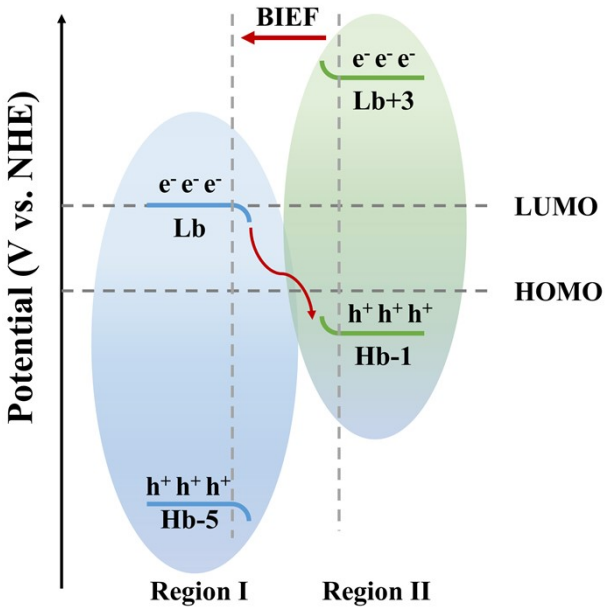

Figure S23. Energy level transition diagram of NDF-OP.

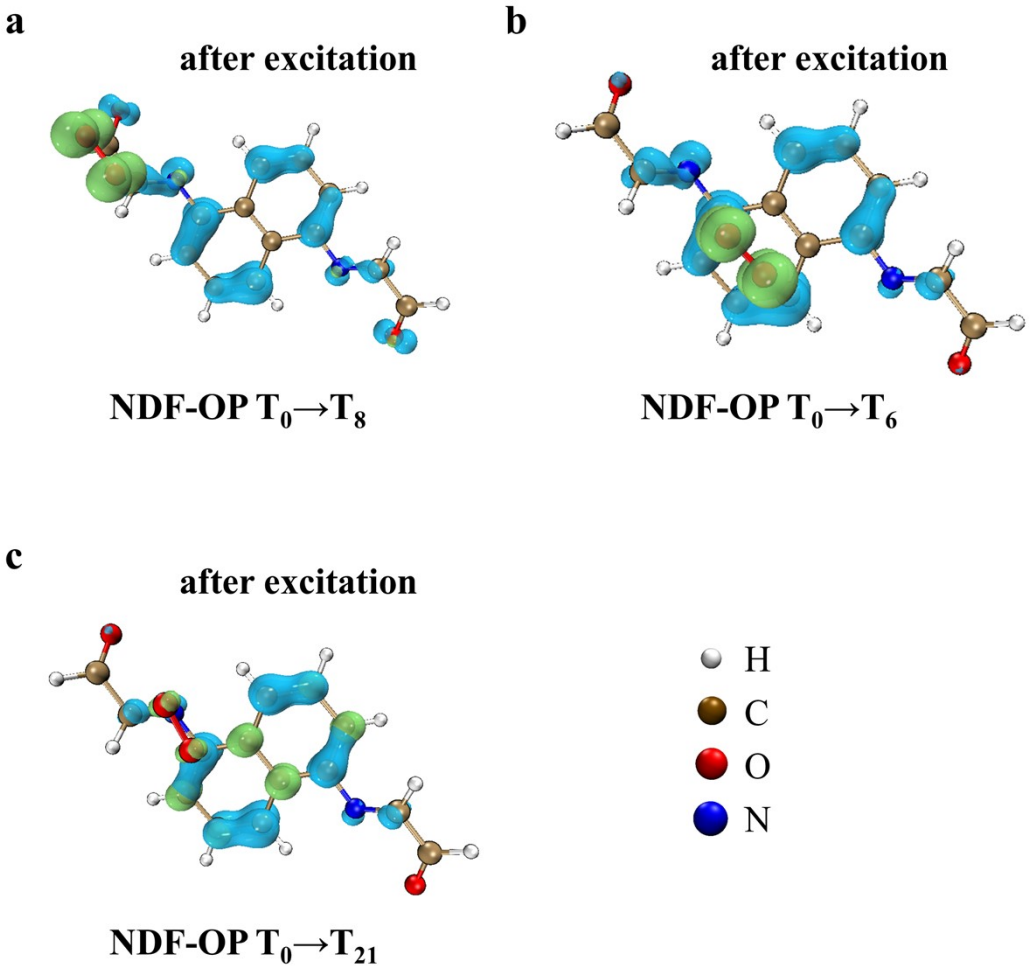

Figure 24. Electron-hole distribution of oxygen adsorbed on NDF-OP under excitation

of (a) $T_0 \rightarrow T_8$ (b) $T_0 \rightarrow T_6$ (c) $T_0 \rightarrow T_{21}$. Green represents the electron distribution and blue represents the hole distribution. The isosurface value is 0.003 e/Å^3.

Table S1 The organic elemental analysis results for NDA-OP and NDF-OP.

Compound	Molecular Formula	C% (Observed/Calculated)	H% (Observed/Calculated)	N% (Observed/Calculated)
NDF-OP	$C_{14}H_{10}N_2O_2$	66.40/66.13	4.26/3.97	13.86/11.02
NDA-OP	$C_{16}H_{14}N_2O_2$	71.68/72.16	4.72/5.30	11.14/12.02

Table S2 Calculated excitation energy (Eexc) and oscillator strength *(f)* at different excited states for NDA-OP and NDF-OP.

Model	excited state	Eexc (eV)	*f* (a. u.)
NDA-OP	$S_0 \rightarrow S_{26}$	5.293	0.1351
NDA-OP	$S_0 \rightarrow S_{23}$	5.129	0.3821
NDF-OP	$S_0 \rightarrow S_9$	3.305	0.1125
NDF-OP	$S_0 \rightarrow S_{24}$	5.133	0.3700

Table S3 Calculated excitation energy (Eexc), oscillator strength (*f*), *t* index and D index at different excited states for O_2 adsorbed at various sites of NDA-OP and NDF-OP.

Model	excited state	Eexc (eV)	*f* (a. u.)	*t* index (Å)	D index (Å)
O2@ NDA-OP (O atom)	$T_0 \rightarrow T_6$	2.994	0.030	3.093	4.677
O2@ NDA-OP (Region II)	$T_0 \rightarrow T_5$	2.751	0.015	0.069	1.369
O2@ NDA-OP (N atom)	$T_0 \rightarrow T_7$	3.117	0.028	-1.852	0.362

O2@ NDF-OP (O atom)	$T_0 \rightarrow T_8$	3.064	0.063	1.708	3.786
O2@ NDF-OP (Region II)	$T_0 \rightarrow T_6$	2.820	0.015	2.067	2.967
O2@ NDF-OP (N atom)	$T_0 \rightarrow T_{21}$	4.181	0.299	-0.796	0.182

References

1. J. G. Chen, C. W. Jones, S. Linic and V. R. Stamenkovic, *ACS Catal.*, 2017, **7**, 6392-6393.
2. C. Kormann, D. W. Bahnemann and M. R. Hoffmann, *Environ. Sci. Technol.*, 1988, **22**, 798−806.
3. J. B. Coulter and D. P. Birnie, *Phys. Status Solidi B*, 2018, **255**, 1700393.
4. Z. Hong, B. Shen, Y. Chen, B. Lin and B. Gao, *J. Mater. Chem. A*, 2013, **1**, 11754-11761.
5. J. Li, G. Zhan, Y. Yu and L. Zhang, *Nat. Commun.*, 2016, **7**, 11480.
6. J. Li, L. Cai, J. Shang, Y. Yu and L. Zhang, *Adv. Mater.*, 2016, **28**, 4059-4064.
7. J. Liu, T. Shen, L. Wang, J. C. Ren, W. Liu and S. Li, *Adv. Funct. Mater.*, 2024, **34**, 2401737.